AD-A147 469 LAMINAR FLOW OVER A BACKWARD-FACING STEP(U) STANFORD UNIV CA CENTER FOR LARGE SCALE SCIENTIFIC COMPUTATION A ZEBIB ET AL. SEP 84 CLASSIC-84-07 1/1

UNCLASSIFIED F/G 20/4 NL

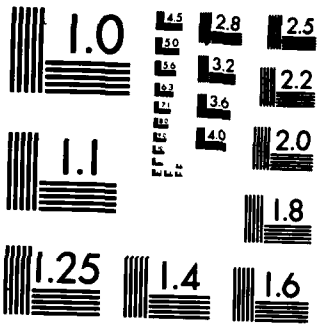
1.0
1.1
1.25
1.4
1.6
1.8
2.0
2.2
2.5
2.8
3.2
3.6
4.0
4.5
5.0
5.6
6.3

ct
aSSiC-84-07

September 1984

inar Flow Over a Backward-Facing Step

by

A. Zebib

G. M. Homsy

Center for Large Scale Scientific Computation
Building 460, Room 304
Stanford University
Stanford, California 94305

ABSTRACT

The steady, two-dimensional flow of an incompressible fluid over a backward-facing step is computed by a finite difference procedure. The flow depends upon the Reynolds number, Re, based on the inlet flow conditions, and on the dimensionless step height, s. Spatially resolved, accurate solutions are obtained for a range of s for Reynolds numbers as high as 350. The primary flow feature is a steady separated region immediately in back of the step. Additionally, a secondary separated vortex can appear on the top, straight wall of the channel. A region is delineated in the (s,Re) plane where laminar separation occurs on the top surface. It is concluded that there is no flow reversal on the top surface if Re is less than about 200, regardless of the step height s. The occurrence of this secondary vortex is associated with laminar separation of the top boundary layer produced by an adverse pressure gradient along the top of the channel.

1. Introduction

The flow field of an incompressible fluid over a backward-facing step exhibits many of the nonlinear features which are intrinsic to viscous fluid motion. Because of this and the frequent occurrence of a sudden expansion in engineering applications, there have been several experimental and theoretical studies of this flow situation. The recent paper by Armaly, Durst, Pereira & Schonung (1983) includes a comprehensive literature review for the problem. Figure 1 is a sketch of the geometry and the possible separated flow structure. The step height is s^* (the superscript * refers to a dimensional quantity) while the gap size is l^*; thus the expansion ratio is $1:(1+s^*/l^*)$. Flow separation occurs at the tip of the step, and the primary eddy reattaches at a distance x_1^* from the inlet. This distance is a function of the expansion ratio and the Reynolds number Re. At sufficiently large Re, secondary separation on the top boundary takes place (see Figure 1) at x_2^* and the flow reattaches at x_3^*. These phenomena were observed by Armaly et al. for an expansion ratio of 1:1.94 and confirmed by the computation of Mansour, Kim & Moin (1983), who compute the flow corresponding to an expansion ratio 1:2.

While the major flow reversal originates due to the sharp edge of the step, it is evident that the top separation comes about, at least in part, because of the adverse pressure gradient associated with the expanding flow created by the dividing streamline (which reattaches at x_1^*). In addition, the Reynolds number of the flow has to be sufficiently large to bring about a boundary layer structure with an associated decrease in the skin friction, which together with the increasing pressure leads to top separation at x_2^* (cf. Brown & Stewartson 1969). However, it should be noted that the adverse

pressure gradient will get weaker with increasing Re as x_1^* increases with Re. Thus, for a given expansion ratio, it may be theorized that top separation, if any, will be confined to a finite range (above zero) of Re.

At sufficiently high Re, Armaly et al. (1983) observe and compute yet another flow separation and reattachment on the lower surface at x_4^* and x_5^* (Figure 1). The discrepancy between their experimental and numerical results however was large. This is due to the large inaccuracy and false diffusion, associated with high Re computations, of the upwind scheme they used. The complicated picture of the flow field sketched in Figure 1, coupled with the fact that the physical model extends to infinity in the flow direction, clearly necessitate the use of a highly nonuniform computational mesh to adequately resolve the different regions of sharp velocity gradients. Such a mesh can be designed after these regions have been identified in exploratory computations. This is the approach we take in this work. However, it is recognized that some form of an adaptive grid refinement may be an attractive and computationally more effective alternative (cf. Berger & Oliger 1984).

The objectives of the present work were to investigate the features of the flow for a wide range of s than is presently available, with particular attention paid to the causes and details of the secondary separation on the top surface.

2. Mathematical model and solution technique

The nondimensional Navier-Stokes equations are

$$\nabla \cdot \underset{\sim}{v} = 0, \tag{1a}$$

$$\nabla \cdot (\underset{\sim}{vv}) = -\nabla p + \nabla^2 \underset{\sim}{v}/Re. \tag{1b}$$

The length and velocity scales are, respectively, l^* and U, where U is the average flow velocity at the inlet. Thus the Reynolds number Re is Ul^*/ν where ν is the kinematic viscosity. Note that this definition of Re is different from that of Armaly et al.. In the usual two-dimensional Cartesian notation, the boundary conditions are

$$\underset{\sim}{v}(0,y) = \begin{cases} (0,0) \quad ; & 0 < y < s, \\ (6(y-s)(1+s-y),0); & s < y < 1+s, \end{cases} \tag{2a}$$

$$\partial_x \underset{\sim}{v}(\infty,y) = 0, \tag{2b}$$

$$\underset{\sim}{v}(x,0) = 0, \tag{2c}$$

$$\underset{\sim}{v}(x,1+s) = 0. \tag{2d}$$

Here s is the nondimensional step length (s^*/l^*) and we have assumed a fully developed parabolic velocity profile at the inlet.

Finite difference solutions of equations (1-2) are computed on the staggered grid shown in Figure 2. The computational region is divided into

rectangular control volumes with the grid points located at the geometric centers of these cells. Additional boundary points are included where the boundary conditions (2) are imposed. The number of the x grid points (control volumes) are NX(NX-2) of which MX control volumes are allocated to a distance $x_L = x_1$. Similarly, the number of y grid points (control volumes) are NY(NY-2) of which MY control volumes are allocated to the gap. As shown in Figure 2, there are two uniform grids in the y direction; the grid covering the primary separated region is also uniform to a distance x_L. The grid increases gradually in the x direction (for a total of NX-2-MX control volumes) to a length nx_L. We set n at 3 which was found to be sufficient by Armaly et al. (1983) and Mansour et al. (1983).

The details of the difference scheme and the iteration procedure we use to solve the difference equations are described by Patankar (1981). The finite difference equations are obtained by integrating equations (1) over the control volumes with assumed local linear variations in all of the primitive variables. The convective and diffusive fluxes are approximated by a power-law scheme. A line-by-line iteration to solve the discretized equations is used with one iteration comprising four double sweeps of the field. Under-relaxation in solving for u and v was required; a relaxation factor of 0.85 was used throughout. Solutions were constructed on a number of non-uniform grids. In Table 1 we list the parameters of 8 such grids together with the VAX 11/780 computer time requirement for one iteration. Convergence was assumed when the maximum change in u or v over one iteration was less than 10^{-5}. About 300 iterations were needed for convergence.

3. Numerical results

a. Numerical accuracy

Solutions of equs. (1-2) were found for a range of (s,Re). Before a specific run, an estimate of x_1 was made in order to ensure a sufficiently long computational region. In Table II we list some of the important details of the flow fields and the particular grid on which that solution is obtained. In Table II ψ is the stream function and x_1, x_2 and x_3 are the values of x where u, computed on the grid line just adjacent to a wall, changes sign. In order to be consistent with previous work, we have expressed these distances normalized with respect to the step height, s.

A general observation from Table II is that finer grids than those used here are needed to produce accurate solutions at the larger values of s or Re. Indeed, the length of the primary bubble x_1 increases with Re at any value of s, at sufficiently low values of Re, as expected. Armaly et al. (1983) report that for s = 0.94, x_1 begins to decrease as Re increases above 200. Mansour et al. (1983), for s = 1, show that this is due to insufficient numerical resolution. Figure 3 shows the dependence of x_1 on Re. We have added our results to those of previous workers, who present results only in graphical form. It is evident that we need a finer mesh than M7 to resolve flow fields above Re = 250 for this range of s. It can also be learned from Table II that if a decrease of x_1 with Re occurs with results from some grid, results with finer grids show that the reverse is correct. Thus the decrease of x_1 with Re reported by Armaly et al. is clearly due to insufficient resolution. It is also interesting that our 80×50 nonuniform mesh apparently gives results for Re $\leq$ 250 which are comparable to those of Mansour et al. who used a 130×130 uniform mesh.

Separation on the top surface, should it occur, may be missed if the grid is not sufficiently fine in the y direction. This is clear from the results listed for s = 0.94 and Re = 200 where results with M3 (30 y-grid points) show no flow reversal while those with M4 (40 y-grid points) indicate top boundary layer separation. Even though the results are not as accurate as we would like to report, it is quite clear that we can state whether the top bubble exists but cannot report more than 2 place accuracy for x_2 and x_3.

In summary, the details of the primary vortex are resolved to an accuracy of 1-2%, and those of the secondary vortex to approximately 10%.

b. **Primary Vortex**

Figure 3 gives our main results on the characteristics of the primary vortex, which for the range of s covered in this study, is of a similar nature to that reported by Armaly et al. and Mansour et al. Our computations do not extend to a sufficiently high Reynolds number to suggest the nature of the eddy growth as $Re \to \infty$. While the experiments of Armaly et al. and theoretical models (see Acrivos & Schrader (1982) for a discussion) suggest that $x_1 \sim Re$ as $Re \to \infty$, no numerical results to date are sufficiently accurate at high Re to allow the question to be unequivocally answered. We do note, however, that since our mesh M4 utilizes a resolution in the primary vortex of comparable quality to the 130×130 uniform mesh of Monsour et al., and since M4 is of insufficient accuracy for Re > 250, the decrease in the rate of growth of x_1 observed by the latter authors is of questionable validity.

c. **Secondary vortex**

Armaly et al. were evidently the first workers to conduct a careful study of the secondary vortex. However their results are for a single value of s, and we became interested in the dependence of the nature and occurrence of secondary separation on this parameter. Our main results are shown in Figure 4, where we plot the approximate locus of the curve in the Re,s plane separating the regions in which the secondary vortex does and does not occur. An interesting feature of this diagram is the double-nosed nature of the curve near $s = 1.0$.

This figure may be understood by first interpreting the limits $s = 0, \infty$. $s = 0$ corresponds to channel flow which evidently has no steady separated regions, regardless of the Reynolds number. Thus the locus cannot intercept the line $s = 0.0$, although it possibly can become tangent to it as $Re \to \infty$. The other limit, $s \to \infty$, corresponds to a wall jet issuing into stagnant surroundings, and again, we have no evidence that steady separated flows exist in that case as well.

As we argued in the introduction, the occurrence of the secondary vortex is most probably a boundary layer phenomenon which will occur, for finite s, for a sufficiently large Reynolds number. The pressure field associated with the deceleration of the expanding flow between the top wall and the zero streamline connecting x_1 with the lip of the step will, at high Re, contain a region of adverse pressure gradient. As the decelerating boundary layer along the top wall is acted upon by viscosity, it will eventually separate, causing a flow reversal and a diminishing of the adverse pressure gradient due to the growth of the secondary vortex.

All of our available numerical evidence is in support of this interpretation. First, we note that in all cases, the point of separation x_2 is upstream of the reattachment point, x_1, of the primary vortex. This is consistent with the above argument since, for $x >> x_1$, the pressure gradient becomes favorable as the flow relaxes to a plane-Poiseuille flow. Second, we can examine the pressure profile on the top wall. Shown in Figure 5 is a series of profiles showing the pressure gradient along the top wall as a function of downstream distance. These particular profiles are for s = 0.8, but other values of s give analogous results. As can be seen, the pressure gradient becomes unfavorable (positive) a short distance from the step. As the Reynolds number increases, the length of the region of unfavorable gradient increases until laminar separation occurs on the top face. This is accompanied by the occurrence of two inflection points in the pressure gradient. Thus comparing Figures 4 and 5, we see that for s = 0.8 Re = 275 is the first case for which two inflection points occur. Above Re = 275, the region of decreasing pressure gradient grows, as does the length of the region between inflection points. This latter behavior is due to the growth of the secondary vortex. These points are emphasized in Figure 5, where for Re = 325 the quantities x_1, x_2, x_3 are marked on the curve. The first inflection occurs at $x \approx x_2$, while the second occurs slightly upstream of x_3. The strong correlation between the pressure gradient and the appearance and disappearance of the secondary vortex is further illustrated by examining the pressure gradient for Re = 225 as a function of s. As can be seen from Figure 4, such a series of profiles traverses regions of separated and unseparated flow twice as s is increased from 0.85 to 1.10. The family of pressure gradient curves is shown in Figure 6, and as can be seen, there is an

excellent correlation between the double inflection points in the pressure gradient and the occurrence of top separation.

From these studies, we may safely conclude that the occurrence of the secondary vortex is a laminar separation of the boundary layer on the top wall due to the adverse pressure gradient set up by the deceleration of the forward moving fluid, which in turn is due to the growth of the primary vortex with Reynolds number.

Some of the detailed features of Figure 4 remain unexplained to us. The occurrence of the nose at $s = 1.05$ may be partially understood by examination of the dependence of x_1 on s at a fixed Reynolds number. Figure 7 shows a number of such curves, and as can be seen, in all cases in which there is to separation ($Re > 200$), x_1 is a local minimum for $s = 1.05$. (The same statement holds true if the quantity x_1/s, as opposed to x_1, is examined.) This indicates that the unfavorable pressure would be expected to be a maximum for $s = 1.05$, leading to separation at the lowest value of Re for which it occurs. The other features of Figure 4 such as the nose at $x_1 = 0.94$, would appear to depend on more subtle details of the flow.

Finally, we note that for $s \sim O(1)$, the secondary vortex cannot grow to be very deep, although it apparently can grow to be quite long. The reason for this is simply that should it penetrate any substantial depth into the channel, it would modify and possibly eliminate the adverse pressure gradient which is responsible for its occurrence. By similar reasoning, the tertiary vortex observed by Armaly et al. is probably a turbulent phenomena, at least for $s \sim O(1)$, since the secondary vortex never grows deep enough to cause a secondary region of decelerating flow, with another associated adverse pressure gradient.

Acknowledgement

We are grateful to the Center for Large Scale Scientific Computation, funded by the Office of Naval Research Contract N00014-82-K-0335 for support and the use of their computer facilities.

References

1. Acrivos, A. & Schrader, M. 1982 Phys. Fluids **25**, 923.

2. Armaly, B.F., Durst, F., Pereira, J.C.F. & Schonung, B.J. 1983 Fluid Mech. **127**, 473.

3. Berger, M.J. & Oliger, J. 1984 J. Comp. Phys. **53**, 384.

4. Brown, S.N. & Stewartson, K. 1969 Ann. Rev. Fluid Mech. **1**, 45.

5. Mansour, N.N., Kim, J & Moin, P. 1983 NASATM 85851.

6. Patankar, S.V. 1981 Numer. Heat Transfer **4**, 409.

Table I
Mesh Definition

Mesh	NX	NY	MX	MY	CPU[1]
M1	30	20	15	9	3.49
M2	40	30	20	14	7.31
M3	50	30	25	14	9.30
M4	60	40	30	19	15.34
M5	70	40	35	19	18.03
M6	80	40	40	19	21.41
M6*	80	40	35	19	21.41
M7	80	50	40	24	32.80

[1] in VAX 11/780 (UNIX) seconds per iteration.

Table II
Variation of results with computational mesh

s	Re	x_L	Mesh	$-100\psi_{min}$	x_1/s	x_2/s	x_3/s
0.7	300	7.5	M4	4.37	10.11		
	325	7.5	M4	4.36	10.61	10.01	11.58
			M5	4.34	10.66	10.05	11.80
			M6	4.32	10.73	10.18	11.86
	350	8.5	M4	4.37	10.92	9.52	13.08
			M5	4.35	11.04	9.68	13.25
			M6	4.33	11.12	9.81	13.35
0.75	275	7.5	M4	4.80	9.69		
	300	7.5	M4	4.79	10.21	9.35	11.51
			M5	4.77	10.26	9.40	11.69
			M6	4.74	10.32	9.50	11.77
	325	8.0	M4	4.79	10.55	9.04	12.95
			M5	4.77	10.66	9.19	13.10
			M6	4.75	10.74	9.30	13.21
0.80	250	7.5	M4	5.22	9.22		
			M5	5.19	9.29		
			M6	5.17	9.33		
	275	8.0	M4	5.23	9.71	8.81	11.08
			M5	5.20	9.80	8.94	11.19
			M6	5.18	9.86	9.03	11.28
	300	8.5	M4	5.24	10.11	8.61	12.45
			M5	5.21	10.22	8.75	12.61
			M6	5.18	10.29	8.85	12.74
	325	9.0	M4	5.25	10.37	8.51	13.54
			M5	5.22	10.51	8.66	13.75
			M6	5.19	10.61	8.78	13.91

Table II (continued)

s	Re	x_L	Mesh	$-100\psi_{min}$	x_1/s	x_2/s	x_3/s
0.85	225	9.0	M4	5.82	8.64		
			M5	5.79	8.68		
			M6	5.76	8.72		
	250	9.5	M4	5.84	9.12	8.02	10.63
				5.80	9.18	8.07	10.84
				5.77	9.23	8.13	10.98
	275	10.0	M4	5.85	9.47	7.86	11.91
			M5	5.81	9.55	7.95	12.15
			M6	5.78	9.62	8.03	12.32
	300	10.0	M4	5.87	9.65	7.74	13.01
		10.5	M5	5.84	9.74	7.84	13.19
		10.0	M6	5.80	9.84	7.95	13.40
0.9	175	8.0	M4	6.25	7.45		
			M5	6.21	7.49		
			M6	6.18	7.52		
	200	9.0	M4	6.28	8.09		
			M5	6.24	8.13		
			M6	6.21	8.17		
	225	9.5	M4	6.30	8.64	7.77	9.77
			M5	6.26	8.69	7.81	9.98
			M6	6.22	8.73	7.85	10.12

Table II (continued)

s	Re	x_L	Mesh	$-100\psi_{min}$	x_1/s	x_2/s	x_3/s
0.94	50	3.0	M1	5.58	3.16		
			M2	5.57	3.17		
	100	3.5	M1	6.53	5.18		
		3.5	M2	6.39	5.12		
		5.0	M2	6.49	5.03		
			M3	6.41	5.07		
			M4	6.35	5.12		
			M5	6.30	5.14		
	150	4.0	M1	6.77	6.35		
			M2	6.60	6.40		
		6.5	M2	6.71	6.67		
			M3	6.63	6.71		
			M4	6.51	6.80		
			M5	6.46	6.83		
			M6	6.42	6.85		
	175	8.0	M4	6.62	7.50		
	200	4.5	M1	6.89	6.44		
			M2	6.68	7.92		
		8.0	M2	6.77	8.00		
			M3	6.69	8.04		
			M4	6.62	8.14	7.86	8.64
			M5	6.58	8.18	7.84	8.84
			M6	6.55	8.22	7.86	8.96
			M7	6.54	8.25	7.87	9.04
	250	9.5	M3	6.76	8.83	7.22	11.09
			M4	6.67	8.98	7.37	11.64
			M5	6.63	9.05	7.44	11.84
			M6	6.59	9.11	7.52	11.99
			M7	6.58	9.17	7.57	12.10
	300	11.0	M3	7.91	8.77	6.80	12.23
			M4	7.20	8.94	6.98	13.01
			M5	6.85	9.06	7.11	13.36
			M6	6.66	9.24	7.26	13.65
			M7	6.64	9.33	7.36	13.86

Table II (continued)

s	Re	x_L	Mesh	$-100\psi_{min}$	x_1/s	x_2/s	x_3/s
0.96	175	8.0	M4	6.68	7.55		
			M5	6.63	7.58		
			M6	6.60	7.62		
	200	9.0	M4	6.70	8.20		
			M5	6.66	8.23		
			M6	6.63	8.27		
	225	9.5	M4	6.70	8.74	7.64	10.25
			M5	6.67	8.77	7.66	10.45
			M6	6.63	8.82	7.72	10.58
	250	8.0	M4	6.64	9.16	7.59	11.82
			M5	6.59	9.27	7.72	11.98
			M6	6.57	9.34	7.80	12.10
	300	9.0	M4	6.67	9.43	7.48	13.51
			M5	6.63	9.54	7.58	13.79
			M6	6.60	9.67	7.70	14.02
	350	9.5	M4	7.76	9.10	7.04	14.11
			M5	7.30	9.25	7.18	14.54
			M6	6.95	9.47	7.37	15.25
1.0	175	8.0	M4	6.50	7.70		
		8.0	M5	6.46	7.74		
		8.0	M6	6.42	7.78		
	200	9.0	M4	6.51	8.46		
		9.0	M5	6.47	8.51		
		9.0	M6	6.44	8.55		
	225	9.5	M4	6.47	9.17		
		9.5	M5	6.43	9.23		
		9.5	M6	6.40	9.28		
	250	9.5	M4	6.38	9.85	9.24	10.54
		10.0	M5	6.39	9.88	9.18	10.77
		10.0	M6	6.36	9.94	9.30	10.86

Table II (continued)

s	Re	x_L	Mesh	$-100\psi_{min}$	x_1/s	x_2/s	x_3/s
1.05	150	8.0	M4	7.54	6.89		
	175	8.0	M4	7.54	7.61		
	200	9.	M4	7.56	8.17	7.06	9.78
	225	9.	M4	7.55	8.55	7.04	11.14
	250	9.0	M4	7.56	8.69	6.97	12.12
	275	12.0	M4	8.78	8.42	6.60	12.26
			M5	8.31	8.51	6.70	12.60
			M6	7.92	8.64	6.81	12.88
	300	12.5	M4	9.76	8.21	6.31	12.42
			M5	9.26	8.31	6.43	12.82
			M6	8.86	8.46	6.57	13.19
1.1	175	8.0	M4	6.74	8.03		
			M5	6.69	8.08		
			M6*	6.86	8.05		
			M7	6.71	8.10		
	200	9.0	M4	6.73	8.90		
			M5	6.69	8.95		
			M6*	6.86	8.90		
			M7	6.72	8.97		
	225	9.5	M4	6.64	9.77		
			M5	6.60	9.84		
			M6*	6.78	9.74		
			M7	6.64	9.84		
	250	10.0	M6	6.56	10.61		
	325	12.5	M4	11.9	7.65	5.78	12.14
			M5	11.1	7.80	5.94	12.65
			M6	10.7	8.06	6.17	13.16
	350	13.0	M4	12.7	7.42	5.51	11.90
			M5	12.2	7.55	5.65	12.41
			M6				

FIGURE CAPTIONS

Figure 1. Sketch of the flow field with regions of flow reversal identified.

Figure 2. The computational nonuniform, staggered grid. There are NX, NY mesh points in the x,y directions, respectively.

Figure 3. The length of the primary vortex, x_1/s, as a function of Reynolds number.

Figure 4. Onset of laminar separation on the top surface. The crosses stand for pairs of (s,Re) where there is no flow reversal while the circles denote separation.

Figure 5. Pressure gradient as a function of downstream distance: s = 0.8 with Re as a parameter. The curves have been shifted in x for clarity.

Figure 6. Pressure gradient as a function of downstream distance: Re = 225 with s as a parameter.

Figure 7. Primary separation distance x_1 as a function of step height s, with Re as a parameter. The error bars denote the maximum error due to the variation of grid sizes among the data plotted.

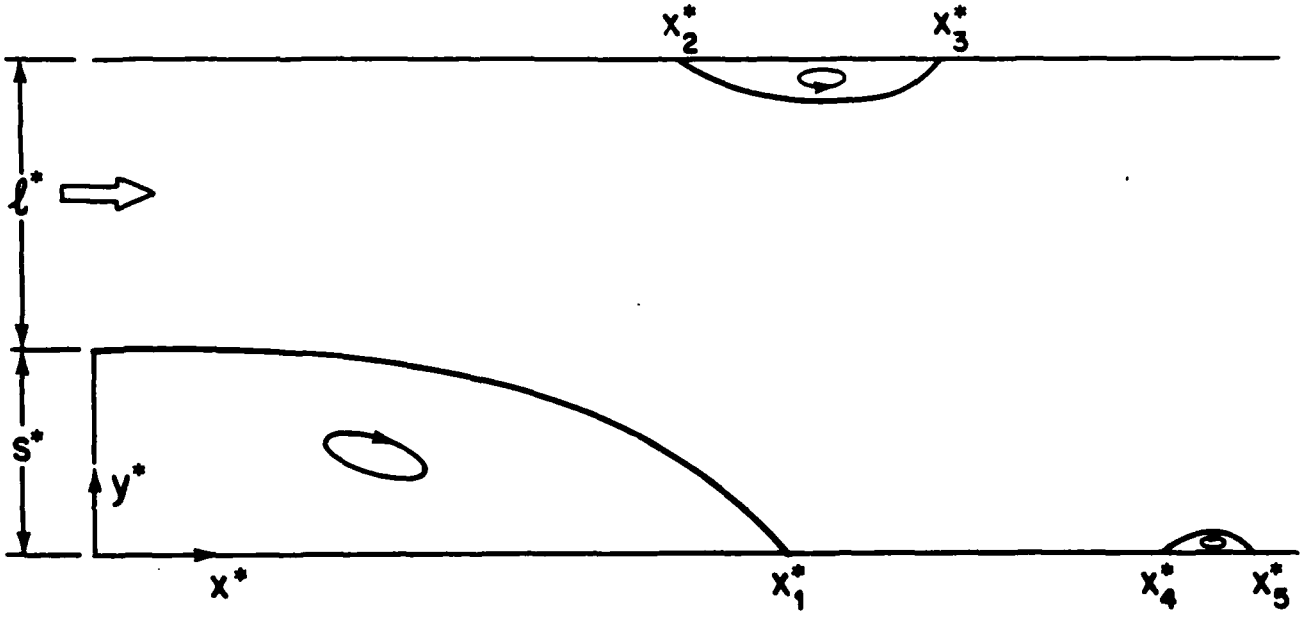

Fig 5.

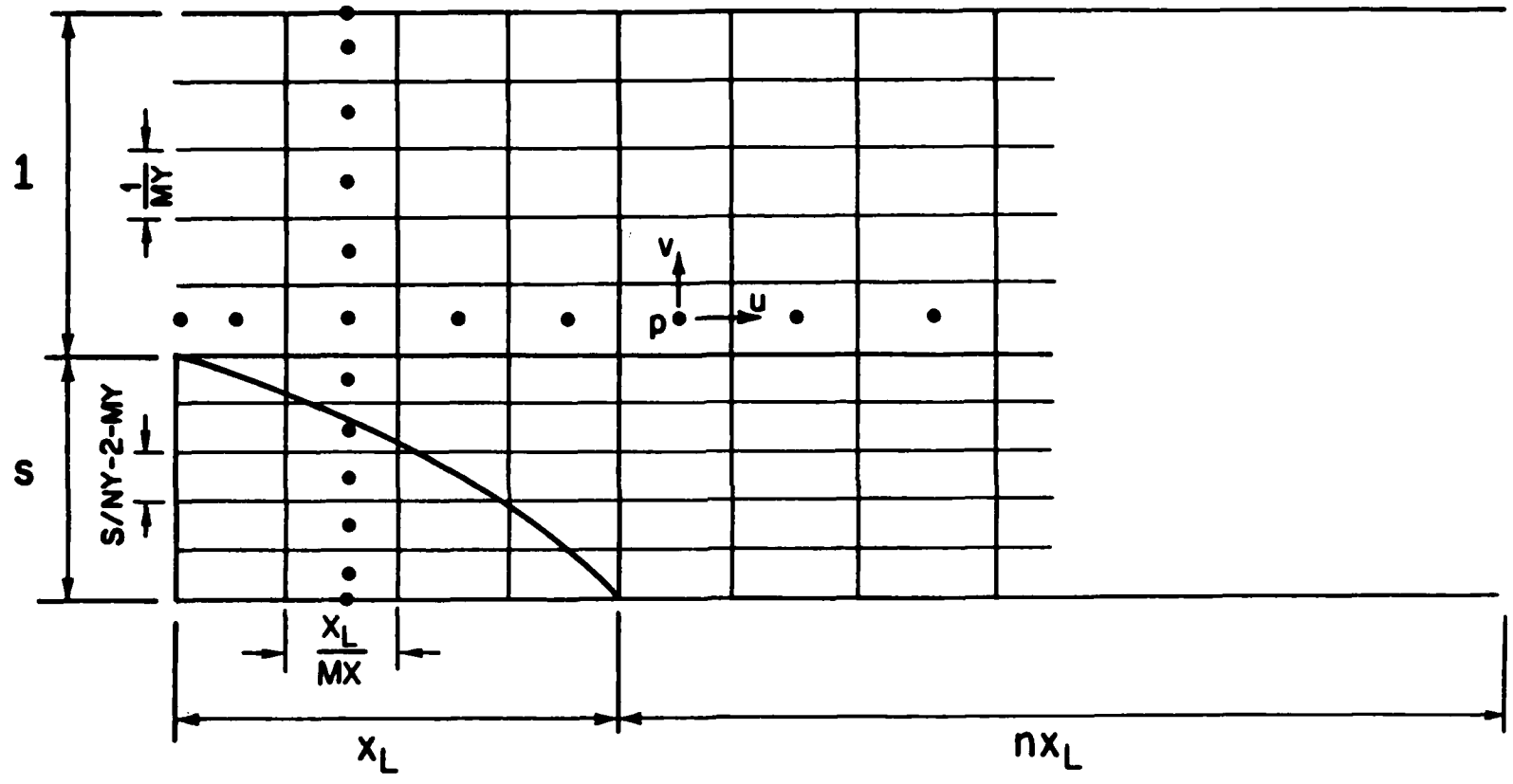
1
$\frac{1}{MY}$
v
p
u
s
S/NY-2-MY
$\frac{X_L}{MX}$
X_L
nX_L

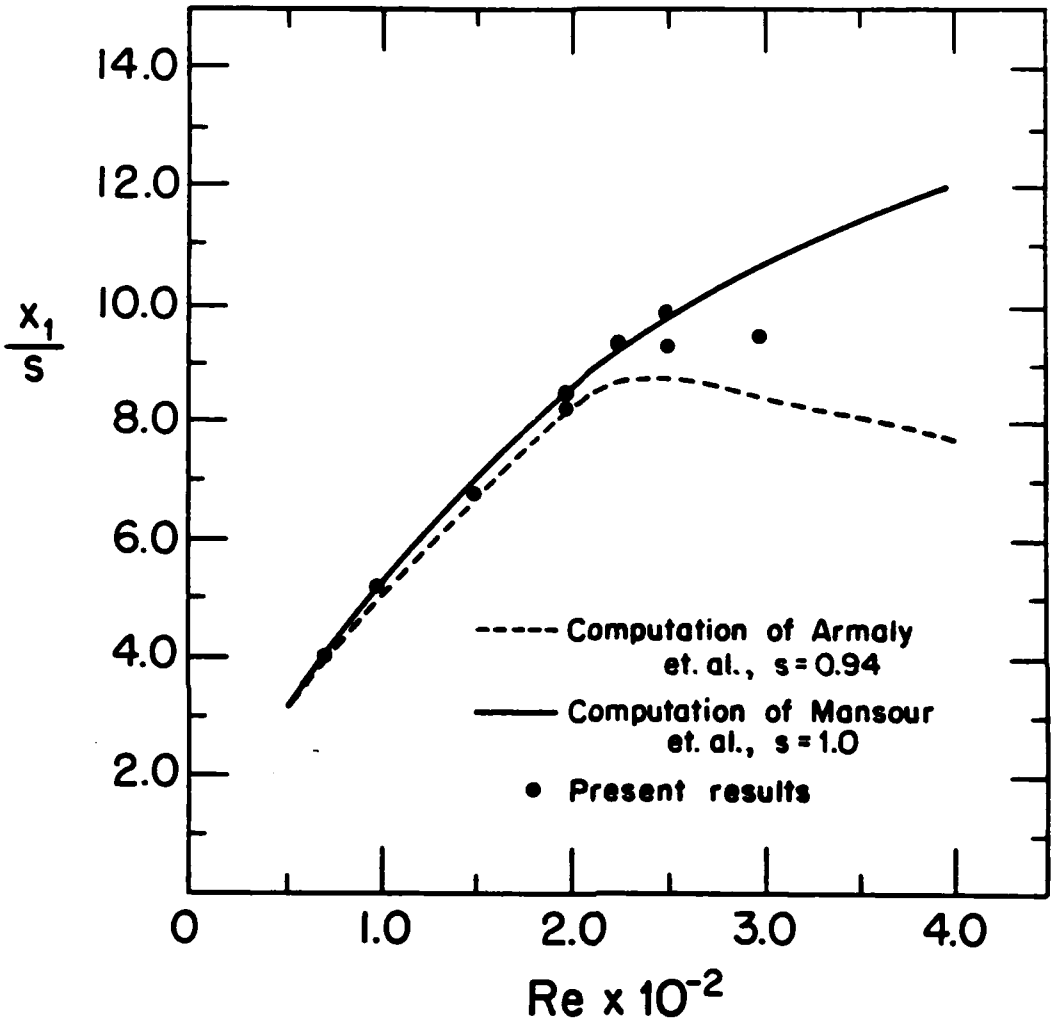
14.0
12.0
10.0
8.0
6.0
4.0
2.0
$\frac{x_1}{s}$
0
1.0
2.0
3.0
4.0
Re x 10^{-2}
----- Computation of Armaly et. al., s = 0.94
—— Computation of Mansour et. al., s = 1.0
• Present results

Fig 3

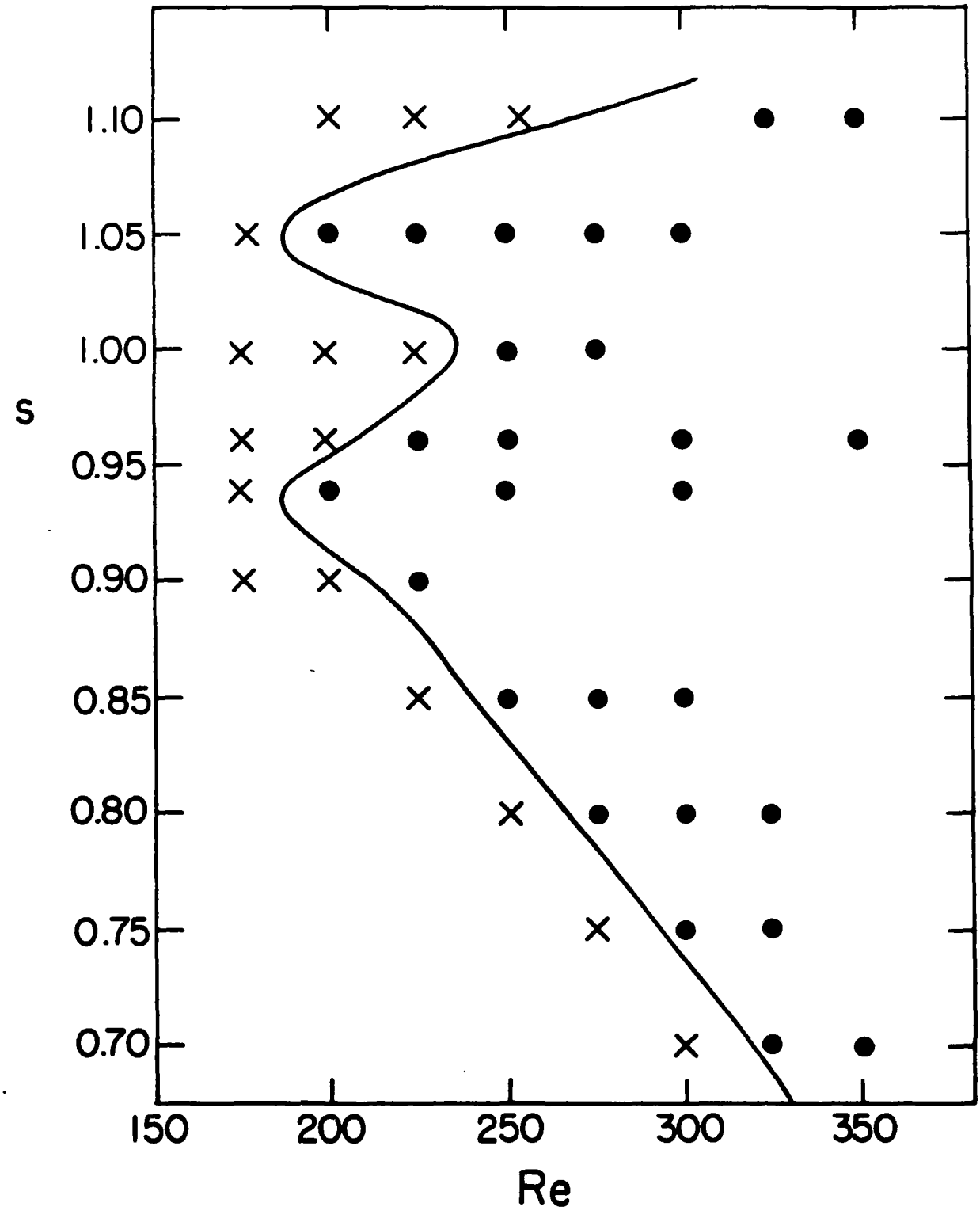
1.10
1.05
1.00
0.95
0.90
0.85
0.80
0.75
0.70
S
150
200
250
300
350
Re

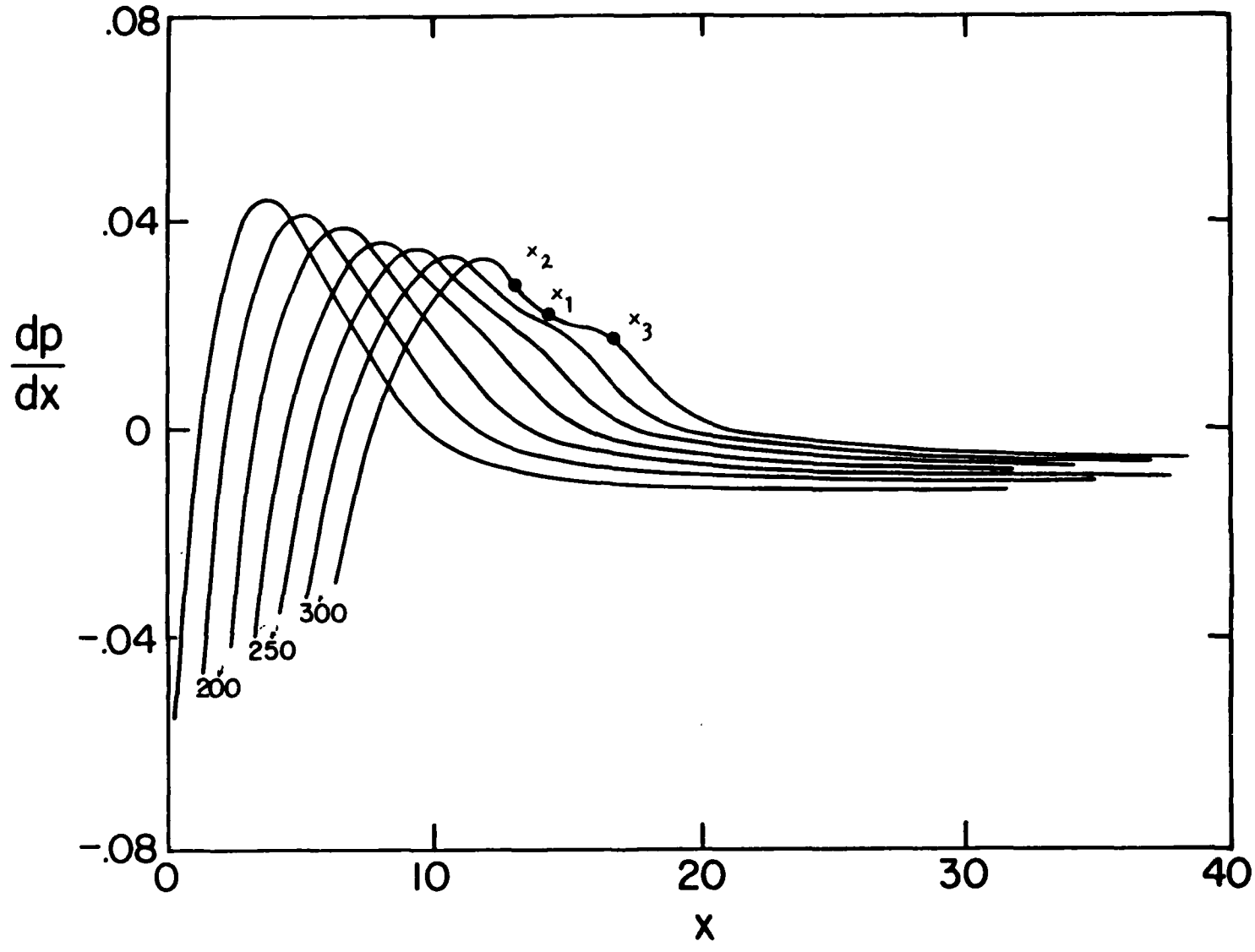
.08
.04
0
-.04
-.08
dp/dx
0
10
20
30
40
x
200
250
300
x2
x1
x3

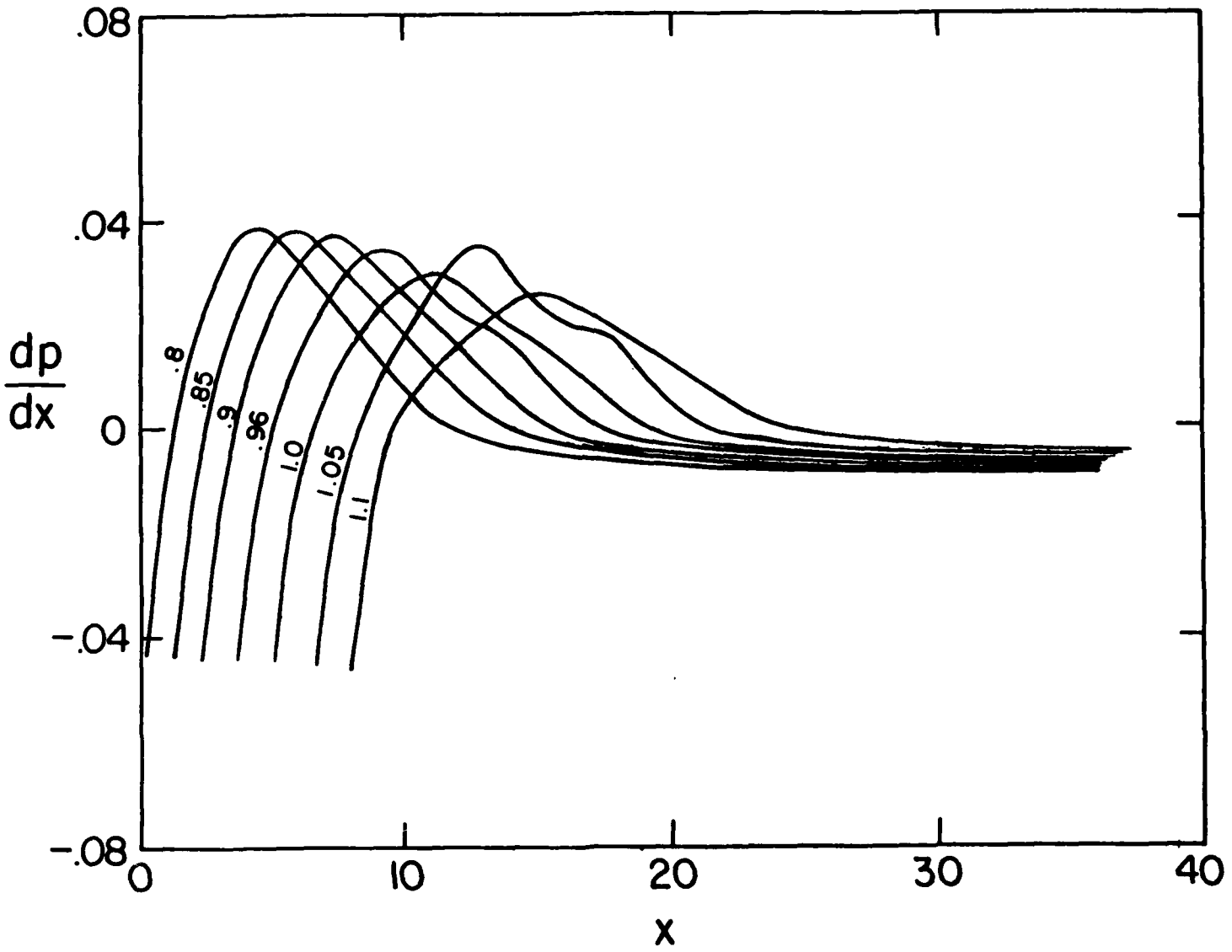
.08
.04
0
-.04
-.08
dp/dx
0
10
20
30
40
x
.8
.85
.9
.96
1.0
1.05
1.1

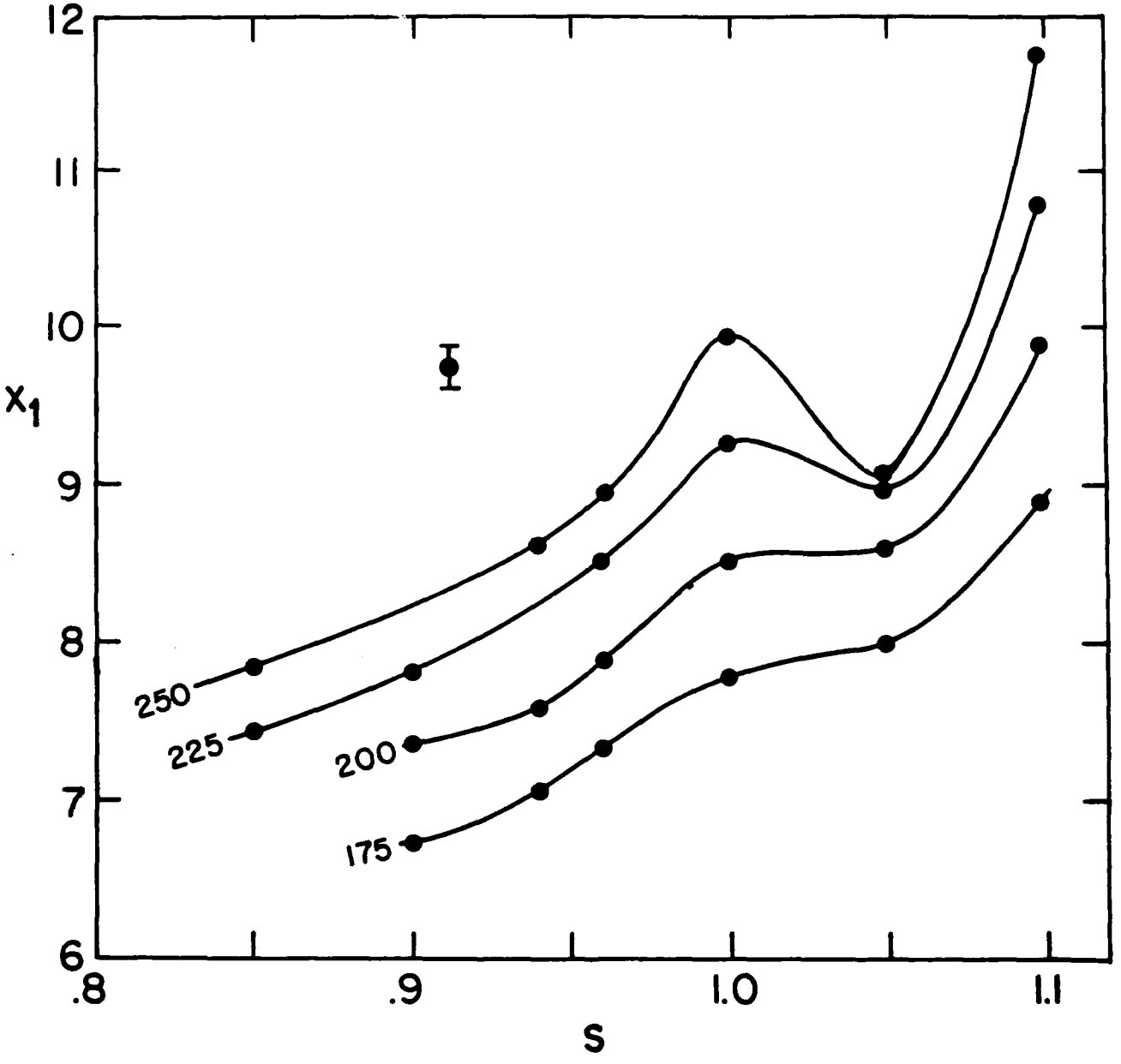
12
11
10
9
8
7
6
x_1
250
225
200
175
.8
.9
1.0
1.1
s

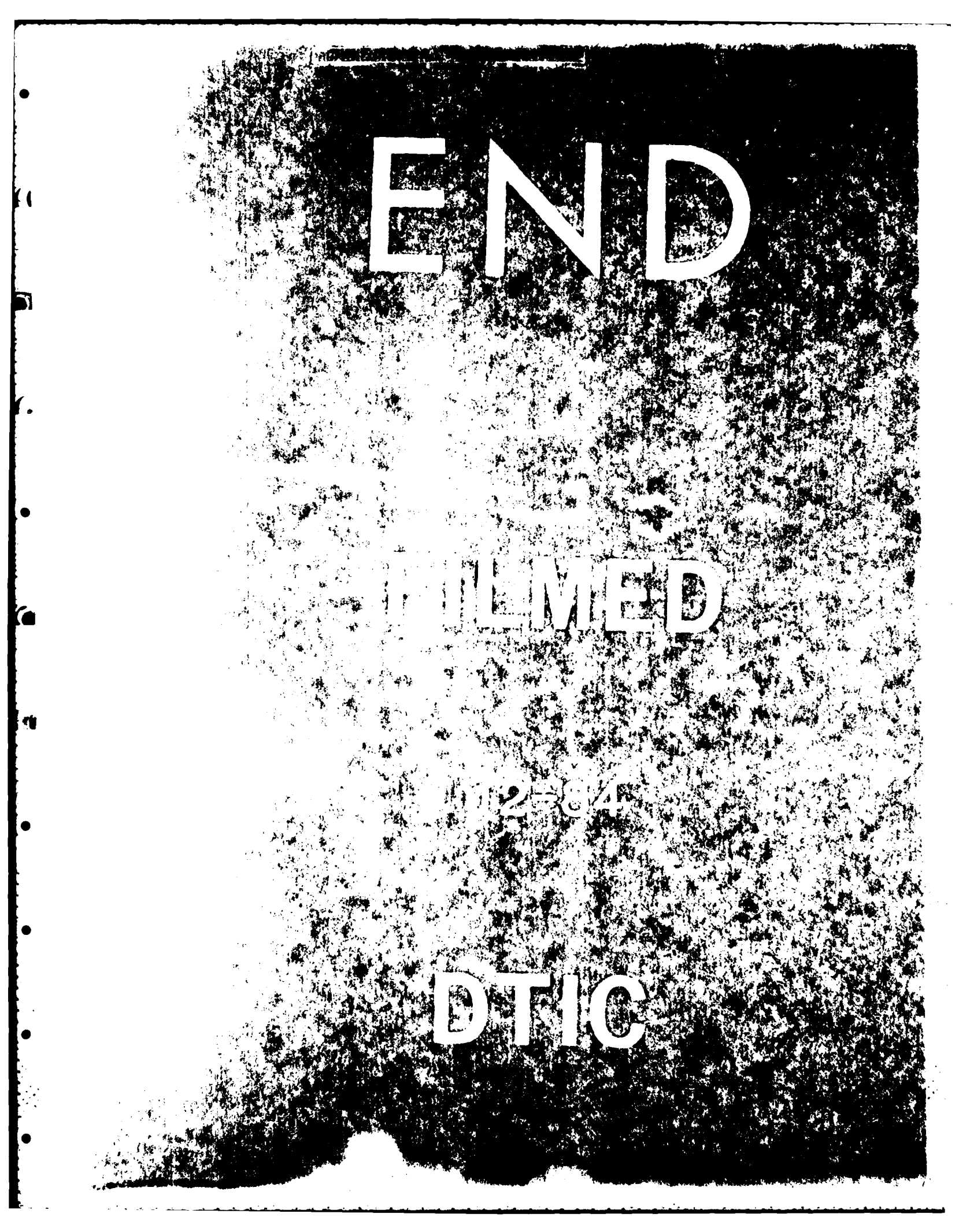
END
LMED
DTIC